ADVANCED ELECTRONIC MATERIALS Open Access
www.advelectronicmat.de

Using Highly Functional Cr_2O_3 Interfacial Layer to Enhance the Electrical Performance of Au/InP Schottky Diodes

Sreedhar Gari Sai Krupa, Dandala Surya Reddy, Ambadi Lakshmi-Narayana, Varra Rajagopal Reddy, and Chintalapalle V. Ramana**

Herein, the significant impact of the spin-coated Cr_2O_3 interface layer on the electrical properties and performance characteristics of Au/undoped-InP (Au/InP) Schottky diodes (SD) is reported. The material characterization of spin-coated Cr_2O_3 films using a wide variety of analytical techniques, namely, atomic force microscopy, field emission scanning electron microscope, X-ray diffraction, Fourier transform infrared spectroscopy, and Raman spectroscopy, indicate the formation of hexagonal phase, nanocrystalline, and stoichiometric Cr_2O_3 on InP. Optical absorption measurements reveal a bandgap of ≈3.5 eV. In-depth analyses and detailed measurements of current-voltage (*I–V*) and capacitance-voltage (C-V) employed to assess the interface characteristics and electrical performance of the Au/InP (SD) versus Au/Cr_2O_3/InP (MIS) devices. Compared to SD, MIS revealed superior rectifying properties. Indicating that the Cr_2O_3 interface layer significantly influences the barrier height (Φ_{BH}) of SD, the estimated Φ_{BH} (0.64 eV (*I–V*)/0.86 eV (C-V)) is higher than that of SD (0.57 eV (*I–V*)/0.67 eV (C-V)). In addition, Cheungs and Nordes' methods are used to obtain the Φ_{BH}, ideality factor (n), and series resistance (R_S). The equivalent Φ_{BH} values obtained from current–voltage, Cheungs, and Nordes methods demonstrate stability and dependability in addition to validating their superior characteristics of MIS devices. The interface state density (N_{SS}) for MIS is lower than the SD's, indicating that the effectiveness of Cr_2O_3 layer significantly reduces N_{SS}. Analyses to probe the mechanism demonstrate that, in SD and MIS, the Schottky emission controls the higher bias area, while the Poole-Frenkel emission dominates the reverse conduction mechanism at the lower bias region. The present work convincingly demonstrates the potential application of the Cr_2O_3 interfacial layer in delivering the enhanced performance and contributes to the progression of electrical devices for emerging electronics and energy-related applications.

1. Introduction

The enormous potential and benefits of metal-semiconductor (MS) contacts in current and emerging micro- to nanoelectronic device technologies, such as field-effect transistors (FETs), phototransistors (PTs), photovoltaics (PVs) and photodetectors (PDs), and other related electronic and optoelectronic devices, have sparked a great deal of research interest in recent decades.[1–7] Semiconductors of the III-V group have been investigated in particular as possible materials in all of the FET, PT, and PD technologies because of their high electron mobility. Among III-V semiconductors, and similar to GaAs, indium phosphide (InP) has been widely used in the design and development of advanced electronics and optoelectronics.[8–13] Due to its comparatively wide bandgap, saturation velocity, and high insulating properties, InP is a feasible material for numerous applications in electronics and optoelectronics.[8–13] InP finds quite interesting applications in high-speed optoelectronic and electronic devices that use a communication wavelength of 1.55 μm as well as high-power microwave devices. Furthermore, its rapid electron mobility makes it an intriguing candidate for fast integrated circuit (IC) technology.[8–14] Additionally, InP-based

S. G. S. Krupa, D. S. Reddy, V. Rajagopal Reddy
Department of Physics
Sri Venkateswara University
Tirupati 517 502, India
E-mail: reddy_vrg@rediffmail.com

The ORCID identification number(s) for the author(s) of this article can be found under https://doi.org/10.1002/aelm.202500050

DOI: 10.1002/aelm.202500050

A. Lakshmi-Narayana, C. V. Ramana
Department of Aerospace and Mechanical Engineering
University of Texas at El Paso
El Paso, TX 79968, USA
E-mail: rvchintalapalle@utep.edu

A. Lakshmi-Narayana, C. V. Ramana
Center for Advanced Materials Research (CMR)
University of Texas at El Paso
El Paso, TX 79968, USA

heterojunction bipolar transistors (HBTs) are one of the highest performance semiconductor devices to date.[14] These HBTs serve the electronics industries in many different ways and, most importantly, are highly desirable for ultrahigh-speed and ultrawide bandwidth digital, analog, mixed signal and radio frequency (RF) applications.[14] In addition to emerging nanoelectronics, InP also finds a wide range of applications in nanophotonics. In fact, highly confined InP photonic membranes enable the design of photonic and photo-active devices.[9–15] InP has been highly successful in the realization of high-performance optical amplifiers integrated with nanophotonic waveguides, which can be easily and directly manufactured on a large scale. InP can also be used in laser diodes and photodetectors and is an ideal candidate for solar photovoltaic (PV) energy conversion technologies.[10,11,15]

In electrical device applications, particularly Schottky diodes (SDs) and related electronic devices, attaining the highest performance is desirable.[4–6,16–18] It has been widely accepted that the performance of SDs is mainly dependent on interfacial conditions, which, in turn, can control electrical characteristics and performance metrics.[4–6,16] In this context, the specific requirement is that SDs must exhibit a high barrier height (Φ_{BH}) and a low leakage current that are crucial to achieve the optimal or best possible device performance.[16] Because metal-induced gap states can result in Fermi-level pinning and surface recombination, direct contact between the semiconductor and the metal can lower the barrier height of the Schottky MS junction.[16–19] For Schottky MS contacts based on InP, despite the potential and greatest promise, the low Φ_{BH} and high leakage current due to Fermi level pinning (FLP) near the conduction band in InP make MS junctions constructed with InP-semiconductors less stable.[17,18] To achieve a low leakage current and high Φ_{BH} in devices based on InP, the addition of an insulating or interfacial layer between the MS contact is a straightforward and beneficial approach. Due to the tunneling barrier that the interface layer creates, this method improves the Φ_{BH}.[7,19] When a thin insulator layer is introduced, the overall structure becomes a metal-insulator-semiconductor (MIS) junction, which typically finds applications not only in electronics but also in energy technologies, particularly in photovoltaics and photoelectrochemical cells.[6,7,19] Therefore, to meet the elevated performance criteria in modern electronic device technologies and also to create more advanced devices for future nanoelectronics and energy technologies, it is necessary to establish an MIS configuration for semiconductors.

The development of MS contacts has been the subject of several research efforts recently, which have improved barrier properties by using various combinations of metal interface layer/insulator (MS and MIS) combinations.[17–25] Erdogan et al. investigated the optical, electronic, structural and morphological transport characteristics of the Cr_2O_3 nanofilm coated on p-Si using the spin-coating technique and identified the electrical protocols.[20] Ocak et al. fabricated Cr_2O_3/n-Si heterojunctions (HJ), measured their optical and electrical characteristics at different substrate temperatures, and reported junction electrical characteristics using current-voltage (*I–V*) and capacitance-voltage (C-V) techniques.[21] Gullu et al. used *I–V* and C-V procedures to investigate the electrical characteristics of spin-coated Al/CrO_3/p-Si and found that the Φ_{BH} was enriched after the inclusion of the CrO_3 interface layer.[22] Balaram et al.[23] used *I–V* and C-V techniques to build an Au/ZrO_2/n-InP MIS diode and established their electrical characteristics. They reported that the Φ_{BH} was improved in the MIS diode. Kim et al.[12] studied the electrical parameters of the Au/Al_2O_3/n-InP junction at different thicknesses of the interface layer and observed an increase in Φ_{BH} equated to the sample without the Al_2O_3 layer regardless of the thickness of the interface layer. Balaram et al.[24] prepared Au/CuO/n-InP HJ and reported that a low leakage current and larger BH were achieved for the HJ compared to the Au/n-InP diode. Salari et al.[25] probed the electrical parameters of the Ag/SnO_2/n-InP Schottky diode using *I–V*/C-V approaches, the reported BH values and the ideality factor were 0.66 eV (*I–V*), 1.32 eV (C-V) and 1.92 respectively. Bilgili[26] studied the correlation between the density of states and the dislocation densities of the Ag/TiO_2/n-InP Schottky diode. The BH with TiO_2 thickness was reported to be 0.524 eV for 60 x and 0.500 eV for 120 x. Thus, the brief review and analysis of the recent literature and efforts directed toward the MIS structures, past and ongoing efforts, contributed to significant advancements in the field. Further, earlier research led to significant advances in the basic knowledge and development of MIS devices for application in electronics and optoelectronics and recently in energy technologies. However, the stability, reliability, high barrier height, and low leakage current remain a technological challenge for the development of InP-based devices for energy, electronics, and optoelectronics.

Transition-metal oxides (TMOs) meet the requirements of interfacial layers.[6,19,27–32] Due to their incredibly intriguing properties, such as their high work function, exceptional transparency, and semiconducting nature, TMOs have recently been used as interface layers for metal interface layer / insulator-semiconductor (MIS) Schottky barrier diodes, organic light-emitting diodes, and other solid-state electronic devices.[6,27,32] Binary TMOs used as oxide/interfacial layers in MS-contacts include V_2O_5,[28;32] MoO_3,[7,32] and WO_3.[29,32] However, while their higher work function may be suitable, the oxides of V, Mo, and W are notable for being strong oxidizing agents, which poses a challenge of chemical instability.[32] In this context, Cr_2O_3 is an important material to consider as an interlayer for the design and development of MIS devices for electronics, electromagnetics, and energy related applications.[33–40]

Cr_2O_3, which is one of the TMOs, is one of the most important transparent *p*-type conducting materials with a wide bandgap (Eg~3.5 eV).[33,38,40] Cr_2O_3 is an important gate-oxide material due to its high hardness (29.5 GPa), its large melting point (2300 °C), excellent wear resistance, chemical inertness, and good resistance to thermal oxidation.[34,35,38] Cr_2O_3 is known to exhibit finite-size effects and flexomagnetic phenomena.[36–38] The ability to control the magnetic order parameter magnetoelectrically made magnetoelectric Cr_2O_3 stand out among the family of insulating antiferromagnets (AFMs).[36–38] In fact, it is unique among known AFMs for electromagnetic applications, as Cr_2O_3 was the first compound in which the linear magnetoelectric effect was theoretically predicted and experimentally confirmed.[36] Recently, Cr_2O_3 has been explored and there is a wide range of interesting applications in energy storage and conversion technologies, such as lithium-ion batteries and supercapacitors.[40,41] Furthermore, compared to oxides of V, Mo, and W, with the highest mechanical strength of any metal and exceptional thermal

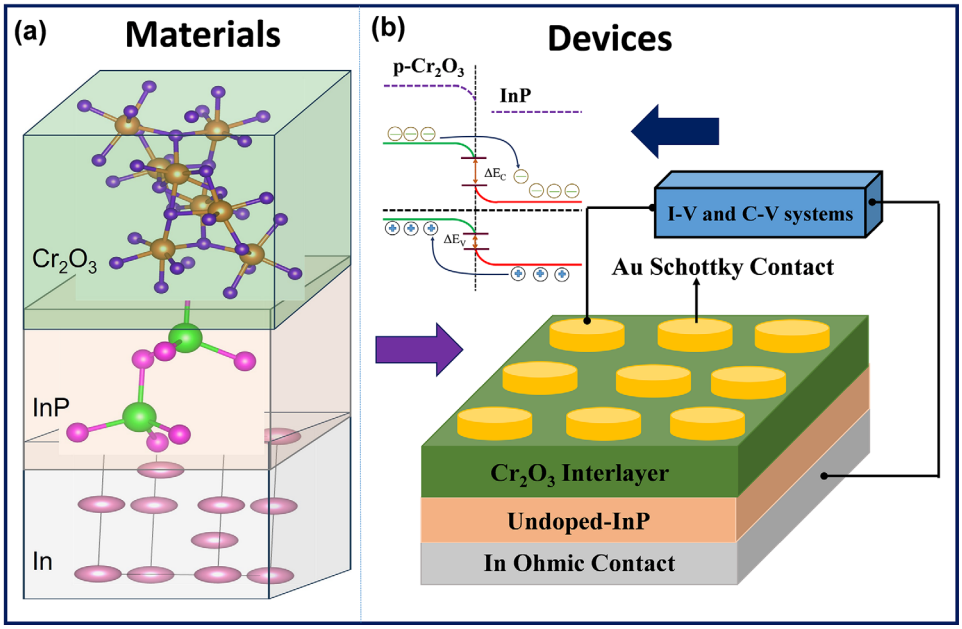

Figure 1. Schematic representation of the Au/Cr_2O_3/InP MIS design involving the Cr_2O_3 interlayer. a) The layout of the materials involved and their stacking are shown. InP and Cr_2O_3 serve as substrate and interfacial layer materials, while Au and In serve as contact materials. b) Schematic representation of the entire MIS device structure.

conductivity, high hardness, chemical stability, high melting point, and resistance to corrosion, Cr_2O_3 exhibits remarkable stability in harsh environmental circumstances.[42,43] Furthermore, Cr_2O_3 has a high dielectric constant (≈12), which is essential for creating insulating layers.[43,44] In field-effect transistors (FETs), a high dielectric constant helps to decrease the electric field between the gate and the channel while increasing the capacitance effect. Furthermore, by doping, the conductivity of Cr_2O_3 can be modified to suit a wide range of uses and produce better electrical transport characteristics. Therefore, it is worth considering Cr_2O_3 as an interfacial layer to design efficient MIS contact structures for electrical device applications. Also, such MIS structures with highly stable dielectric (Cr_2O_3) in conjunction with highly desirable semiconductor (InP) may open up a new horizon in the field of electronics. Furthermore, undoped InP often exhibits a weakly n-type behavior due to slight unintentional doping,[45] which can still form an effective p-n junction with the p-type Cr_2O_3 layer. This approach provides a more controlled built-in field, allowing for efficient charge separation without the potentially excessive field that might arise from a heavily doped n-type substrate. Additionally, the use of undoped-InP helps minimize interface states and reduce recombination losses, resulting in a cleaner interface and improved charge transport across the junction. This is the motivation for the present work to design materials for MIS structures using Cr_2O_3 as an interfacial layer (see **Figure 1**). As presented schematically in Figure 1, we considered InP and Cr_2O_3 as the main materials while Au, In as contact materials (Figure 1a), while the entire device was manufactured as shown in Figure 1b. The significance of the present approach is the use of a phase-controlled Cr_2O_3 interfacial layer in the engineering of Au-Cr_2O_3-InP devices with desirable electrical properties and performance. Therefore, in our work, due to the notable features of Cr_2O_3, we fabricated the Au/Cr_2O_3/InP metal/interface layer/semiconductor Schottky-type diodes using a simple, economically viable spin coating process for the Cr_2O_3 interface layer. First, we performed the comprehensive material characterization of spin-coated Cr_2O_3 thin films on InP surfaces, where the goal was to validate and ascertain the phase, structural quality, and chemical bonding in Cr_2O_3 films. A wide variety of analytical methods, namely atomic force microscopy (AFM), field emission scanning electron microscopy (FESEM), X-ray diffraction (XRD), Fourier transform infrared (FTIR), Raman spectroscopy, and X-ray photoelectron spectroscopy (XPS), were employed for the purpose. Then, using UV-vis-NIR spectrometry measurements and analyses, the bandgap and optical absorption properties were evaluated. Finally, the electrical features and performance of the MIS diodes were evaluated by detailed *I–V* and C-V measurements along with modelling of the data. The electrical characteristic parameters, such as the ideality factor (n), barrier height (Φ_{BH}), series resistance (R_S) and interface state density (N_{SS}), were determined. Comparative analyses of Au/InP and Au/Cr_2O_3/InP were performed to highlight the effect of Cr_2O_3 and the consequences of MIS compared to SD in devices based on InP.

2. Results and Discussion

2.1. Material Characterization – Surface Morphology, Structure, Chemical Bonding, and Surface Chemistry

2.1.1. Atomic Force Microscopy (AFM) and Field Emission Scanning Electron Microscopy (FESEM)

The surface morphology and cross sectional interface structure of spin-coated Cr_2O_3 thin films on an InP substrate were analyzed using atomic force microscopy (AFM) and field emission

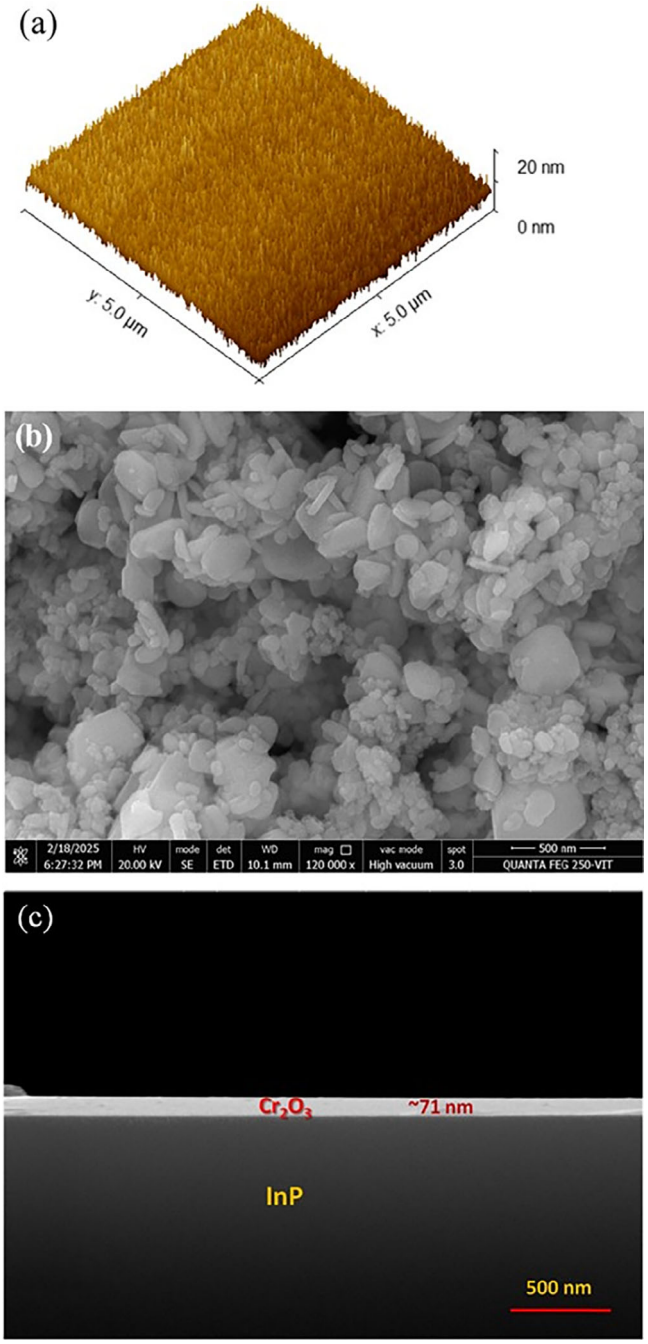

Figure 2. a) 3D AFM images of Cr_2O_3/InP layer. b) Top view SEM image for surface morphology and c) cross sectional view for layer thickness of the Cr_2O_3 film deposited on the InP substrate.

scanning electron microscopy (FESEM) measurements. The 3D AFM micrograph of the Cr_2O_3 film is presented in **Figure 2a**. The surface topography of the Cr_2O_3 films was examined within a scanning area of 5 µm × 5 µm. The surface morphology of the Cr_2O_3 thin films is considerably smooth, with a root mean square (RMS) roughness of 2.74 nm. Figure 2b,c shows the FESEM images of the Cr_2O_3 thin film deposited on the InP substrate, highlighting the surface and cross sectional details of the layers, respectively. The surface morphology shown in Figure 2b reveals the formation of nanosized grains that are uniformly distributed across the surface. The AFM and SEM results corroborate indicating the nano-grain surface morphology of the Cr_2O_3 films. The cross section of the Cr_2O_3/InP layers, illustrated in Figure 2c, indicates the presence of a Cr_2O_3 interlayer of ≈71 nm thickness over the well-defined InP layer. Additionally, a consistent thickness of the Cr_2O_3 layer is observed throughout the micrograph region. Additionally, the InP-Cr_2O_3 interface structure is characterized by dense overlayer film while there is no obvious interfacial reactions or irregularities that can detected in the SEM cross sectional images. Thus, the surface and interface microstructure examination.

2.1.2. X-Ray Diffraction

The XRD pattern of the Cr_2O_3 film on the undoped-InP is shown in **Figure 3a**. It is evident that the pattern displays diffraction peaks indicating the crystalline nature of the Cr_2O_3 film. The peaks due to Cr_2O_3 overlayer and InP are indicated in Figure 3a. The peaks at 2θ values of 33.3°, 35.9°, 44.3°, 54.5°, 64.85°, and 76.2° corresponds to the diffraction of (104), (110), (202), (116), (300), and (220), respectively, Cr_2O_3 planes (as confirmed by JCPDS no: 00-038-1479). The identified peaks and their indexing of the diffraction planes clearly indicate the formation of the hexagonal structure of Cr_2O_3 (Figure 3b) with a primitive rhombohedral cell. This is in good agreement with the literature, where analogous peaks were identified by Ponmudi et al.[46] Also, the diffraction peaks are observed at 51.9° and 72.5° are related to diffraction from the (311) and (420) planes of the InP substrate (JCPDS: 01 073 1983). These peaks and their 2θ values planes are similar to those reported in the literature.[47] However, while the resulting Cr_2O_3 films are nanocrystalline, no specific texture was observed. For Cr_2O_3 thin film, depending on the processing conditions, thickness, and underlying substrate material, texturing or preferred orientation may be possible, particularly for deposition at higher temperature. Perhaps, the optimum temperature required to promote the growth of a crystalline film on InP may be the reason, and it is desirable in our approach. Therefore, the XRD data evidence that phase pure formation of spin-coated Cr_2O_3 film on InP stabilizes in the hexagonal phase without any secondary phase ascertaining phase formation and the absence of impurities or impurity phases. For electronic device applications, achieving phase-pure and nanocrystalline Cr_2O_3 films is quite important, as impurities or secondary phases can degrade electrical characteristics and/or device performance.

2.1.3. Raman Spectroscopy and Fourier Transform Infrared Spectroscopy

Vibrational spectroscopic characterization, particularly the combined approach based on Raman spectroscopy (RS) and Fourier infrared spectroscopy (FTIR), is quite useful for examining chemical bonding and structural quality in bulk and thin-film materials.[48–50] Both RS and FTIR are nondestructive, do not require any specific sample preparation, and have shown great promise in evaluating the chemical bonding and structural integrity of both basic and complicated materials.[50] Therefore, to

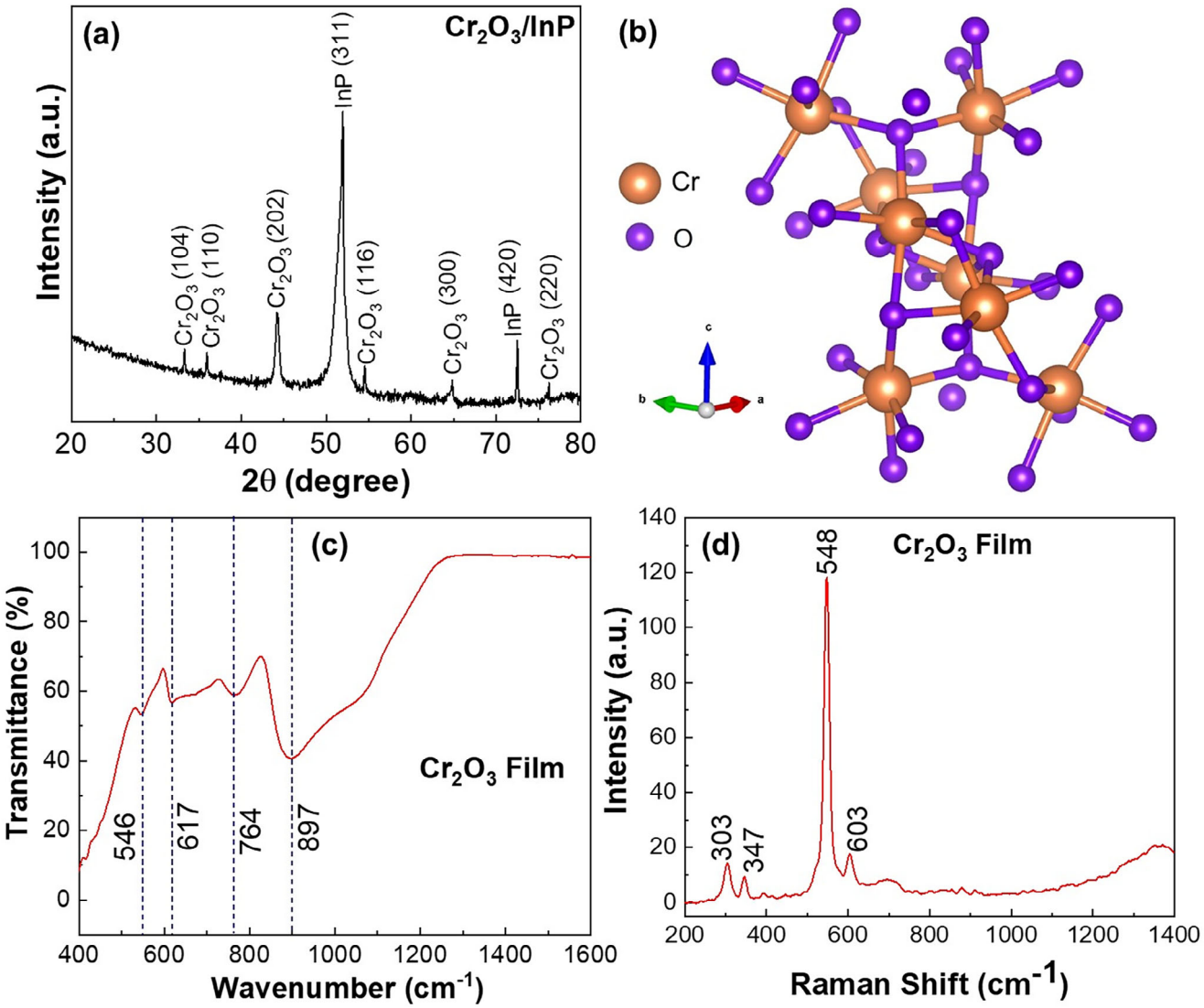

Figure 3. a) XRD pattern of Cr_2O_3 films in InP. The peaks due to Cr_2O_3 film and those related to InP substrate are as indicated. The indexing of the peaks confirms the formation of hexagonal Cr_2O_3. b) Crystal structure of hexagonal Cr_2O_3. c) FTIR spectrum of Cr_2O_3 films. The observed FTIR bands and their positions are indicated. d) Raman spectrum of Cr_2O_3 films. The Raman scattering bands observed and their positions are indicated.

understand the structural configuration and/or chemical bonding of Cr_2O_3 films on InP, we relied on in-depth FTIR and Raman spectroscopic evaluation of the materials. The FTIR and Raman data of Cr_2O_3-InP are presented in Figure 3c,d, respectively. The FTIR spectrum, which is measured in the range of 400–1600 cm^{-1}, shows the distinct vibrational bands at 546, 617, 764, and 897 cm^{-1}. The observed bands are well correlated with earlier reports.[43,51–53] The vibrational bands observed at 546 and 617 cm^{-1}, which are attributed to E_u vibrational modes,[43,51] define and ascertain the crystalline quality of the material.[15] Furthermore, the band observed at 764 cm^{-1} ascribed to the Cr-O elongating modes. The existence of this characteristic band also confirms the crystallinity of Cr_2O_3 thin films.[52] The vibrational band detected at 897 cm^{-1} could be due to Cr = O vibration.[52,53] On the other hand, the Raman spectrum (Figure 3d), which is measured in the wavelength range of 200–1400 cm^{-1}, also exhibits the characteristic bands that can be exclusively assigned to Cr_2O_3. The bands observed in the Raman spectra are located at 303, 347, 548, and 603 cm^{-1}. In Cr_2O_3, two active vibration modes are defined and are attributed to $A_{1\ g}$ and E_g vibrations.[51] The most intense vibration observed at 548 cm^{-1} can be attributed to the $A_{1\ g}$ regularity mode due to the Cr-O vibration in the rhombohedral Cr_2O_3,[52] whereas the other vibrational modes are contributed by the E_g symmetry modes.[51,52]

2.1.4. X-Ray Photoelectron Spectroscopy

To examine the chemical characteristics of the Cr_2O_3 layer on InP, the XPS technique is utilized. The high purity of Cr_2O_3/InP film is evidenced by the peaks seen in the survey spectra (not shown), which validate the presence of intense Cr and O peaks.

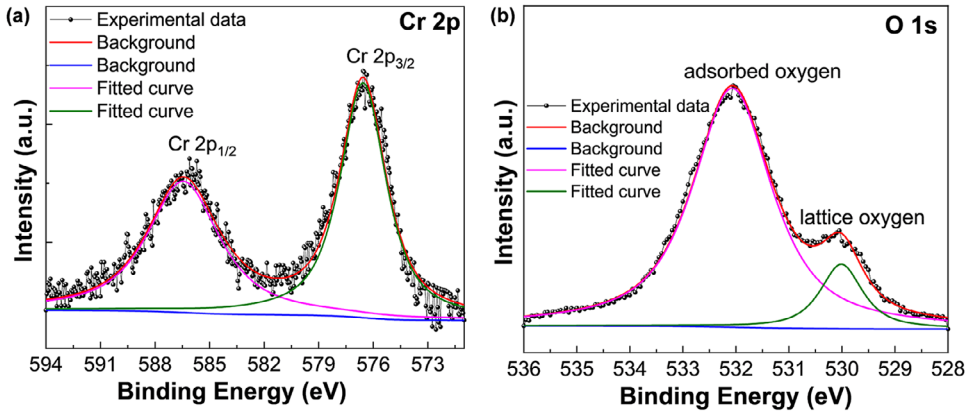

Figure 4. XPS data of Cr_2O_3 films. The data shown are the detailed core-level scans of: a) Cr 2p and b) O 1s. The data of Cr 2p (a) indicate the existence of Cr ions in their highest chemical valence state. The deconvluted O 1s core level spectra (b) indicate that oxygen may appear in a variety of chemical states, including oxygen bonded to Cr and hydroxyl groups (OH). The asymmetric nature of the O 1s peak is also evident.

Figure 4a displays the Cr 2p core-level photoelectron spectra, where it is clear that the Cr 2p peak exhibits a doublet. The peak shape and binding energy (BE) values of the doublet, which correspond to the spin-orbit splitting components of Cr $2p_{3/2}$ and Cr $2p_{1/2}$, clearly match those found for stoichiometric Cr_2O_3. Peaks (Figure 4a) observed at BE~586.45 and 576.55 eV are due to Cr $2p_{1/2}$ and Cr $2p_{3/2,}$ respectively.[40–42,54] Thus, in spin-coated Cr oxide, the existence of Cr ions in their maximum chemical valence state (Cr^{3+}) confirmed by the Cr $2p_{1/2}$ and Cr $2p_{3/2}$ peaks.

Figure 4b shows the deconvoluted spectra of O 1s, which contains two distinct peaks, observed at BE of 532.05 and 530.05 eV, which corresponds to the adsorbed oxygen and lattice oxygen respectively.[55] The O 1s spectra indicate the complex chemistry as a result of the surface sensitive nature of XPS and also the exposure of the sample prior to introduction into the XPS chamber. Although the broadness of the peak accounts for the lattice oxygen and surface adsorbed oxygen components, the asymmetric behavior of the O 1s peak is also clearly seen. The second peak, observed ≈532 eV, corresponds to the OH^-/H_2O species physisorbed on the surface. This indicates that, in addition to the XPS signal from lattice oxygen, two distinct signals originate from two types of water interacting with the surface of the substance. One signal is due to hydroxyl group, which is chemisorbed, facilitated by lattice defects or vacancies, while the other signal arises from physisorbed water molecules that experience dipole-dipole interactions with the lattice oxygen.[56] The most important aspect is the Cr-O peak, located at 530.05 eV, which can be ascribed to the Cr-O bonds in Cr_2O_3. The ratio of Cr: The O in the deposited Cr_2O_3 is determined to be 2.01: 2.96 (Cr: O) based on the peak area ratios of the Cr 2p and O 1s core-level XPS spectra, accurately reflecting the actual stoichiometry of the Cr_2O_3 compound.

The XPS data of the substrate are also acquired and shown in the Supporting Information. In 3d core level spectra (Figure S1, Supporting Information) are comprised of dual spin-orbit split peaks; the less strong peak with a higher BE of 452.05 eV is ascribed to In $3d_{3/2}$, while the high strong peak has less BE of 444.5 eV is ascribed to In $3d_{5/2}$. Similarly, the core-level spectra of P 2p (Figure S2, Supporting Information), which is composed of two spin-orbit peaks. The highest BE (129.6 eV) is assigned to P $2p_{1/2}$, while the lowest BE (128.75 eV) is recognized to be P $2p_{3/2}$.[57] Thus, the XPS analyses reveal the stoichiometric nature of the materials with the existence of respective cations in their expected chemical valence state.

2.2. Optical Properties

The data obtained in the optical measurements of the Cr_2O_3 films are presented in **Figure 5**. The spectral transmittance of the Cr_2O_3 films is shown in Figure 5a, where the trend of optical absorption is also presented for direct comparison. The sharp increase in transmittance corresponds to the optical absorption across the fundamental bandgap of the films. The corresponding absorption data (Figure 5a) indicate a strong absorbance in the near-UV region, while the absorbance decreases with increasing wavelength. The optical bandgap of Cr_2O_3 films was evaluated using the relationship of absorption coefficient (α) and photon energy ($h\nu$) relation as depicted by Tauc's relation:[58]

$$[\alpha h\upsilon] = B\left[h\upsilon - E_g\right]^n \quad (1)$$

where $h\nu$ is the energy of the incident photons, B is the energy-independent constant and E_g is the bandgap of the material. The magnitude of the exponent "n" defines the nature of the optical transitions involved (n = 1/2, 2 define the direct and indirect allowed transitions, respectively). The Tauc plot, which is the plot between $(\alpha h\nu)^2$ versus photon energy, obtained from the absorption spectra is shown in Figure 5b. It is evident that the data fit well with the exponent n = 1 / 2, validating the optical transitions in Cr_2O_3. Extrapolation of the edge of the band to the x-axis reveals the direct optical bandgap of the Cr_2O_3 films. It is evident from Figure 5b that the optical bandgap of the Cr_2O_3 films was estimated to be ≈3.5 eV, which is comparable with those reported in the literature.[20,21,43] In Cr_2O_3, the valence band (VB) is primarily composed of oxygen 2p orbitals, while the conduction band (CB) is mainly made up of Cr 3d orbitals, with a large bandgap. The energy separation between VB and CB classifies Cr_2O_3 as a wide band-gap semiconductor. However, the presence of impurities and/or dopants, which results in the formation of

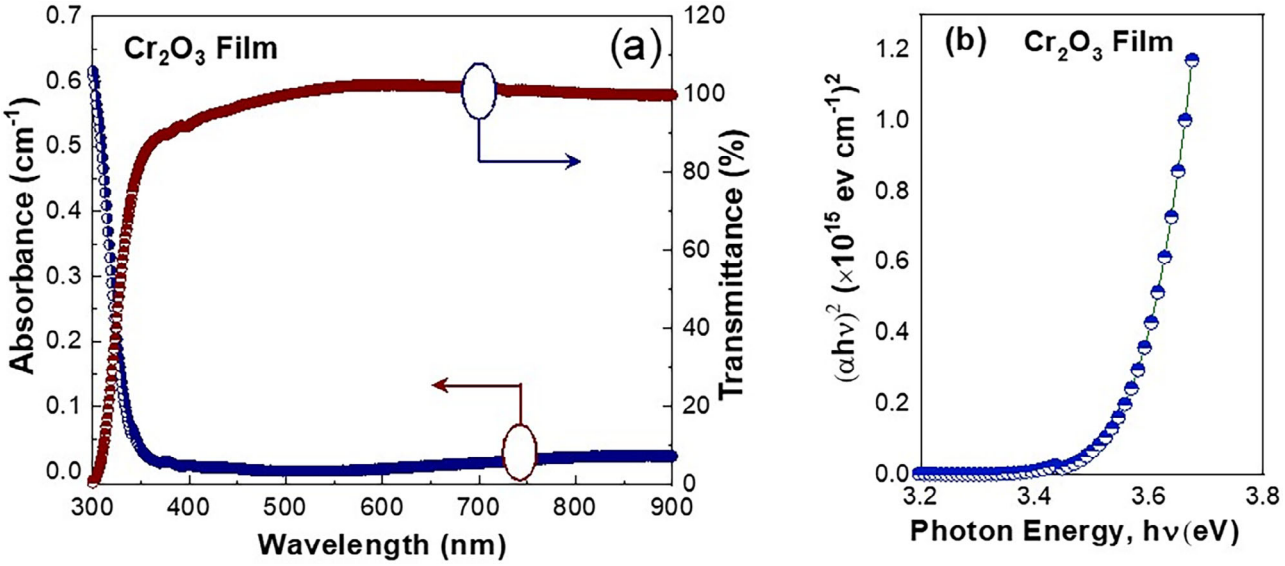

Figure 5. Optical absorption data of Cr_2O_3 films. The data shown are: a) UV–vis absorption and transmittance spectra of Cr_2O_3 films; and b) Tauc's plot to evaluate the optical bandgap of Cr_2O_3 films.

localized states within the bandgap, can significantly lower the E_g values, leading to compromising the desired electrical properties. Therefore, in agreement with XRD, FTIR, and Raman spectroscopic measurements, optical absorption measurements also indicate the formation of phase-pure Cr_2O_3 films. We also determined the indirect bandgap of Cr_2O_3 films by means of the Tauc's plot (Figure S3, Supporting Information). The Tauc's plot for indirect bandgap also followed the same procedure, i.e., plotting the absorption data as a function on energy and extrapolating the linear region to the zero absorption. The indirect bandgap estimated is ≈3.4 eV, which is lower in magnitude compared to direct bandgap. This observation is also in reasonable agreement with the literature.[59,60] Furthermore, the magnitude of indirect bandgap (≈3.4 eV) estimated in this work for spin-coated Cr_2O_3 films is comparable to the value (≈3.3 eV) reported for Cr_2O_3 films made by other methods.[59,60]

2.3. Electrical Properties and Performance

2.3.1. Current-Voltage (I–V) Characteristics

To explore the impact of the Cr_2O_3 layer on the electrical properties of Au/InP Schottky diode (SD), the Au/Cr_2O_3/InP metal/interface layer/semiconductor (MIS) Schottky type diode is constructed with a Cr_2O_3 interface layer. The *I–V* and C-V characteristics were studied in-depth. **Figure 6a** presents the *I–V* features of the SD and MIS diodes, where the notable effect of the Cr_2O_3 interfacial layer on the electrical characteristics is evident. The measured rectification ratio at ±1V for SD (8.82) and MIS (17.12) indicates the establishment of a depletion zone at the Cr_2O_3/InP interface. The reverse leakage current at -2 V for MIS (6.557×10^{-6}A) is much lower compared to that of SD (4.269×10^{-5}A). The results demonstrate that the electrical possessions of the MIS are enriched by the addition of a Cr_2O_3 layer within the MS junction. The feeble voltage dependence of the reverse bias current and the exponential rise of the forward bias current are the distinguished features of the rectifying contacts. The bending at a higher current in the log(I)-V plot for the forward bias regime cab can be attributed to the series resistance of the contacts or the bulk resistance of the Cr_2O_3 and InP.[20] Furthermore, the observed non-saturation nature as a function of the applied voltage in the reverse bias regime of SD and MIS was attributed to the reduction of barrier height (Φ_{BH}) as well as the presence of native oxides or the interface layer at the SD interface.[61] The relationship between I and V can be stated as:[62]

$$I = I_0 \left(\exp\frac{q(V - IR_S)}{nkT} - 1\right) \text{ here } I_0 = AA^*T^2\exp\left[\frac{-q\Phi_{BH}}{kT}\right] \quad (2)$$

$$\Phi_{BH} = \frac{kT}{q}\ln\left[\frac{AA^*T^2}{I_0}\right] \quad (3)$$

$$n = \frac{q}{kT}\left[\frac{dV}{d(\ln I)}\right] \quad (4)$$

Here I_0, A (1.96×10^{-3} cm^2), R_S, V, T, k, q, A^* (9.4 A cm^{-2} K^{-2}[3]), n and Φ_{BH} have standard denotations.[63] The Φ_{BH} and n can be derived from the intercept and slope of the linear area of the forward bias *I–V* plot. The Φ_{BH} and n values determined from the *I–V* plot are 0.57 eV and 1.31 for the SD, while they are 0.64 eV and 1.27 for the MIS contact. The higher Φ_{BH} value obtained for MIS compared to SD is due to the reduced electron tunneling and leakage current at the Cr_2O_3/InP junction. More precisely, the notable effect of the Cr_2O_3 interfacial layer is reflected in the promotion of higher Φ_{BH}. The mechanism involved can be explained as follows. The Cr_2O_3 layer at the interface creates a physical barrier between the overlayer Au and the underlying InP semiconductor interface, inhibiting reaction and interdiffusion in the MS contact. Furthermore, the bending of the semiconductor band could be due to

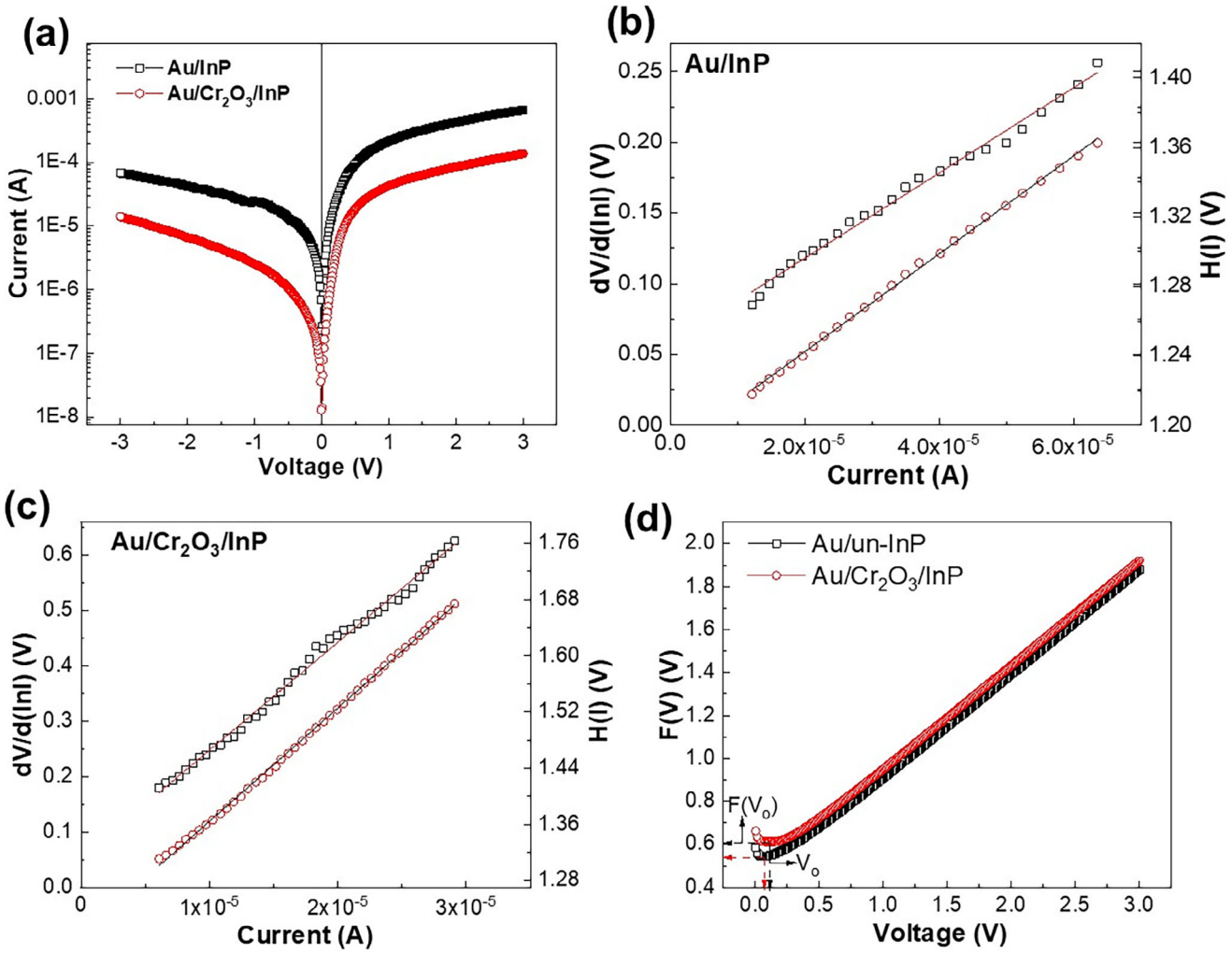

Figure 6. Current-voltage (*I–V*) data of Au/Cr_2O_3/InP MIS devices. The data shown are: a) The *I–V* characteristics of the Au/InP SD and Au/Cr_2O_3/InP MIS devices; b) The dV/dlnI versus I and H(I) versus I plot of Au/InP SD devices; c) The dV/dlnI versus I and H(I) versus I plot of Au/Cr_2O_3/InP MIS devices; d) The F(V) versus V plot for the Au/InP SD and Au/Cr_2O_3/InP MIS devices.

the interaction between the metal and oxide-modified substrate leading to the overall modification in the Φ_{BH}.[23] Furthermore, the "n" values measured from the *I–V* plot for SD and MIS were greater than unity. The highest values of "n" can be attributed to the potential drop through the interface layer, the presence of native oxides, series resistance, and excessive current in the interface states at the Cr_2O_3/InP junction. The regulation of metal-induced gap states and the bias voltage dependence of Φ_{BH} at the interface may contribute to the increase in "n". Additionally, other possible factors include the image force effect, the distribution of interface states, and the processes of generation recombination and tunneling. Lateral inhomogeneous Φ_{BH} might be accountable for the larger "n" values.[23]

Further analysis of the *I–V* plot can be performed using the Cheungs method. As seen from Figure 6a, the non-linear curvature in the higher voltage range of the forward bias *I–V* plot for both SD and MIS could be due to the influence of series resistance (R_S) and interface states (N_{SS}) that are in equilibrium with the InP semiconductor.[20] Thus, Cheungs' technique was applied to evaluate R_S, Φ_{BH} and n for both SD and MIS in the non-linear regime. Cheungs' equations[64] are defined as:

$$\frac{dV}{dlnI} = IR_S + n\left(\frac{kT}{q}\right) \tag{5}$$

$$H\ (I) = V - n\left(\frac{kT}{q}\right)\ln\left(\frac{I}{AA^{*}T^{2}}\right) \tag{6}$$

Also,

$$H\ (I) = IR_S + n\Phi_{BH} \tag{7}$$

Equations (5) and (6) give the straight line for the nonlinear data of the forward bias log(I)-V plot. The dV/dlnI versus I and H(I) versus I plots for SD and MIS are shown in Figure 6b,c, respectively. The plot dV / dlnI versus I (Figure 6b,c)) provides R_S from the slope and "n" from the y-axis intercept for both SD and MIS structures. The evaluated values of R_S and "n" are 3.0 kΩ

and 2.23 for SD, 19.5 kΩ and 2.08 for MIS, respectively. The significant improvement in the R_S value observed for MIS is due to the Cr_2O_3 layer at the interface. The value "n" obtained from the graph dV / dlnI versus I is substituted into Equation (6), the graph H (I) versus I is drawn, where the linear fit of the curve provides R_S from the slope and Φ_{BH} from the intercept of the y-axis. The corresponding values of the R_S and Φ_{BH} values obtained from the H(I) versus I plot are 2.2 kΩ and 0.53 eV for SD and 18.1 kΩ and 0.61 eV for MIS. The R_S values predicted from the dV/dlnI versus I and H(I) versus I plots are in good correlation with each other, confirming the consistency and efficiency of the Cheungs approach. Therefore, the implemented Cheungs approach validates the overall effect of the Cr_2O_3 interface layer on the electrical characteristics of the MIS. However, in contrast, the "n" values assessed by the Cheungs technique are different from those found in the *I–V* plot. This could be due to the impact of R_S, the density of states, the bias dependency of the Φ_{BH} and the voltage drop across the Cr_2O_3 interface layer.[20] Additionally, the Φ_{BH} values obtained from the H(I) versus I plot are nearly analogous to the values achieved from the *I–V* plot with forward bias.

Furthermore, Nordes proposed an alternate process to determine R_S and Φ_{BH} for SD and MIS diodes. The Nordes' function[65] can be expressed as:

$$F\ (V) = \frac{V}{\gamma} - \frac{1}{\beta}\ln\left(\frac{I}{AA^{*}T^{2}}\right) \text{ here } \beta = q/kT \tag{8}$$

here γ is the dimensionless integer higher than "n" attained from the *I–V* plot, "I" is the current considered from the *I–V* data. The Φ_{BH} can be calculated from the equation:

$$\Phi_{BH} = \left[F\left(V_0\right) + \frac{V_0}{\gamma} - \frac{kT}{q}\right] \tag{9}$$

Here, $F(V_0)$ is the lowest value of F(V) and V_0 is its respective voltage. Figure 6d shows the F(V) versus V plot of SD and MIS. Furthermore, the R_S can be derived from the expression:

$$R_S = \left(\frac{kT}{q}\right)\left(\frac{\gamma - n}{I_0}\right) \tag{10}$$

where I_0 is the respective current for the lowest value of $F(V_0)$. The acquired values of the R_S and Φ_{BH} values are 3.5 kΩ and 0.56 eV for SD, 28.0 kΩ and 0.64 eV for MIS, respectively. The magnitudes of Φ_{BH} magnitudes from the *I–V* plot, the Cheungs and Nordes approaches are analogous to each other, revealing the reliability and precision of the procedures. The distinction in R_S magnitudes attained from Cheungs and Nordes techniques is owing to the different forward bias *I–V* regions utilized. The Cheungs technique is limited to the nonlinear portion, while Nordes method covers the whole forward-bias regime.[20]

2.3.2. Capacitance-Voltage (C-V) Characteristics

The capacitance-voltage (C-V) and C^{-2} versus V characteristic plots of the Au/InP SD devices are shown in **Figure 7a**, while the C-V and C^{-2} versus V characteristic plots of the $Au/Cr_2O_3/InP$ MIS devices are shown in Figure 7b. The C-V relation is conveyed as:[66]

$$\frac{1}{C^2} = \left(\frac{2}{\epsilon_s q N_d A^2}\right)\left(V_{bi} - \frac{kT}{q} - V\right) \tag{11}$$

Here, N_d, A, ϵ_s and V_{bi} have usual notations.[67] The $\Phi_{BH,\ C\text{-}V}$ and built-in potential (V_{bi}) for SD and MIS could be derived from the C^{-2} versus V plot. The values obtained of V_{bi} and $\Phi_{BH,\ C\text{-}V}$ are 0.61 V and 0.67 eV for SD and 0.81 V and 0.86 eV for MIS, respectively. The results revealed that the Φ_{BH} appraised from the C-V procedure is greater than those acquired from log(I)-V data. This could be due to barrier inhomogeneities, trap states in the depletion layer, a thin interface layer and charges in surface states.[10] Another reason might be due to the spatial variation of Φ_{BH}, MS contact is rough rather than atomically flat. The capacitance does not respond to spatial fluctuations that occur on a scale less than that of the space-charge area. Furthermore, current flow in the *I–V* method occurs primarily through barrier minima, leading to a reduction in the Φ_{BH}.[23] **Table 1** summarizes the Φ_{BH}, n and R_S for the SD and MIS diodes. Some of the reported Φ_{BH} values of InP-based MIS/MOS type devices are given in Table 1 for comparison.

It is evident from Figure 6a that both the SD and the MIS display nonlinearity in the upper forward bias voltage region of the *I–V* curves. This behavior indicates the presence of a continuum of interface state density (N_{SS}) that is in equilibrium with the semiconductor. Card and Rhoderick[66] stated that N_{SS} can be defined as follows:

$$N_{SS} = \frac{1}{q}\left[\frac{\epsilon_i}{\delta}\left(n\left(V\right) - 1\right) - \frac{\epsilon_s}{W_D}\right] \tag{12}$$

here δ, $n(V) = qV/[kT\ \ln(I/I_0)]$ and W_D have regular notation.[24] Moreover, the energy of interface states (E_{SS}) relative to the conduction band edge (E_C) at the undoped-InP surface can be stated as:

$$E_C - E_{SS} = q\left[\Phi_e - V\right] \tag{13}$$

Here, V and Φ_e are the voltage drop through the depletion layer and the effective barrier height, respectively. The voltage dependence of Φ_e includes the ideality factor (n) as:

$$\frac{d\Phi_e}{dV} = 1 - \frac{1}{n\left[V\right]} = \beta \tag{14}$$

where

$$\Phi_e = \Phi_{BH} + \beta\left(V\right) \tag{15}$$

here "β" is the voltage coefficient.

The N_{SS} versus (E_C-E_{SS}) diagram for SD and MIS is shown in Figure 7c,d. The N_{SS} displayed exponential growth with a bias from mid-gap to the lowest section of the conduction band. The acquired N_{SS} magnitudes for SD and MIS are shown in Table 1. The results show that the MIS has a lower N_{SS} value than the SD, which means that the Cr_2O_3 layer significantly decreases the N_{SS}. The results reveal that the Cr_2O_3 layer has a momentous

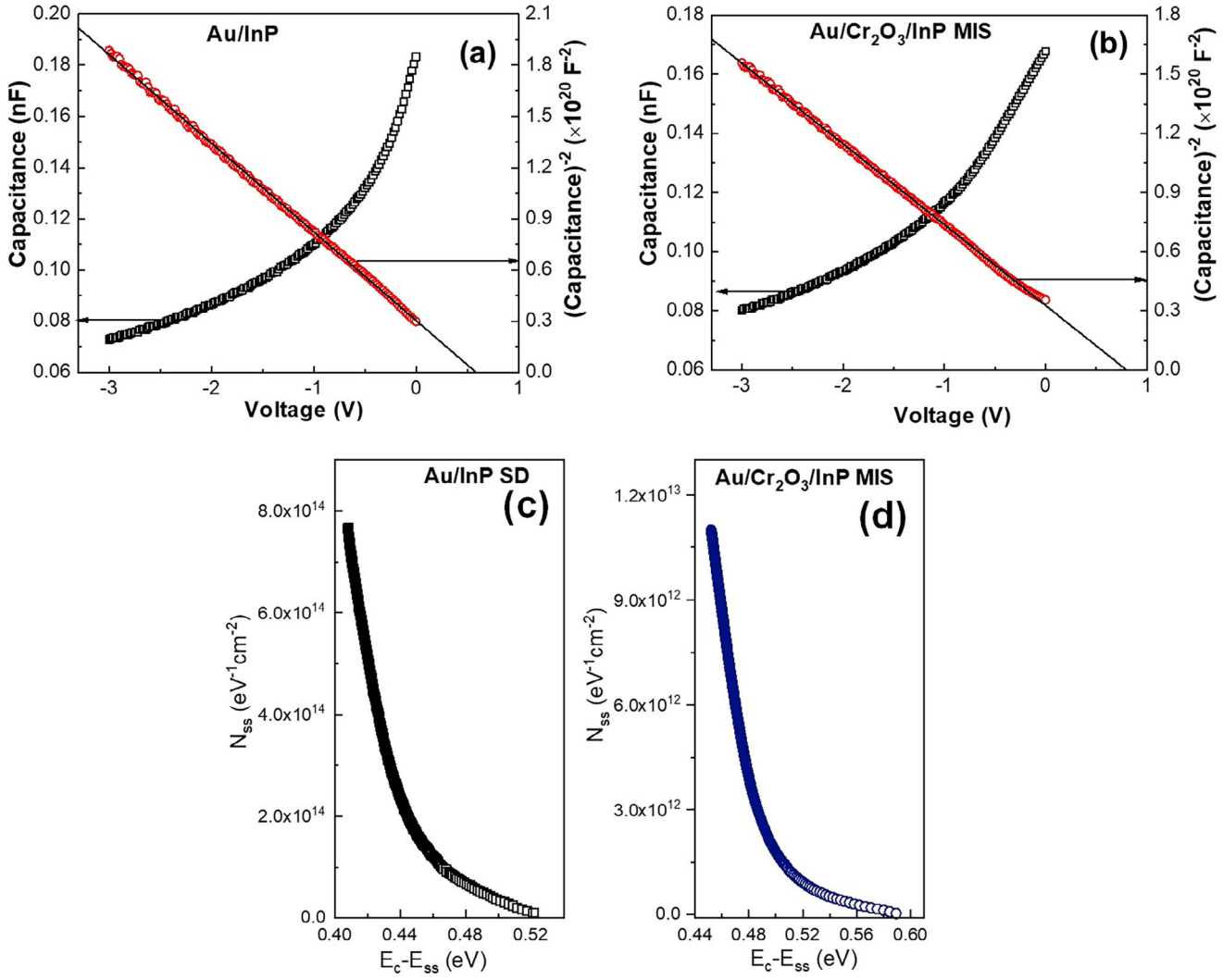

Figure 7. Capacitance-voltage (*I–V*) data of Au-InP SD and Au-Cr_2O_3-InP MIS devices. The data shown are: a) The C-V and C^{-2} versus V characteristic plots of the Au/InP SD devices; b) The C-V and C^{-2} versus V characteristic plots of the Au/Cr_2O_3/InP MIS devices; c) The N_{SS} versus E_C-E_{SS} diagram of the Au/InP SD devices; and d) The N_{SS} versus E_C-E_{SS} diagram of the Au/Cr_2O_3/InP MIS devices.

influence on the interface states, although the Cr_2O_3/undoped-InP junction remains abrupt and unreactive. This implies that the Cr_2O_3 layer successfully passivates the undoped-InP surface, thus decreasing the deep electronic states present on the undoped-InP semiconductor surface and subsequently reducing the N_{SS}.[23] As a result, the Cr_2O_3 layer improves the Φ_e of SD and reduces the reverse leakage current.[24] Therefore, it might be confirmed that the Cr_2O_3 interface layer impacts the N_{SS}.

2.3.3. Energy Band Structure and Mechanism

Figure 8a shows the energy band structure of the Au/Cr_2O_3/InP junction. To draw an energy band structure, the respective values of the energy bandgap (E_g) and the electron affinities (χ) for the p-Cr_2O_3 semiconductor and the undoped-InP semiconductor are considered. The values are: $\chi_{Cr2O3} = 3.93$ eV,[71] $E_{g,Cr2O3} = 3.5$ eV,[20] $\chi_{InP} = 4.38$ eV, $E_{g,InP} = 1.34$ eV. The variation between the top of the valence band and the lower region of the conduction band of InP and p-Cr_2O_3 is measured. The conduction band offset (CBO) obtained is $\Delta E_C = \chi_{InP} - \chi_{Cr2O3} = 4.38 - 3.93 = 0.45$ eV and the valence band offset (VBO) is $\Delta E_V = E_{g,InP} - E_{g,Cr2O3} + \Delta E_C = 1.34 - 3.4 + 0.45 = -1.61$ eV. The results indicate that the energy band structure shows a higher CBO and a lower VBO.

Finally, we performed analyses to understand the reverse-current conduction mechanism in both SD and MIS devices. Following standard practice, that is, by examining the Poole-Frenkel emission (PFE) and Schottky emission (SE),[72] the reverse-current conduction mechanism (RCM) of SD and MIS devices is analyzed. If the reverse current is governed by PFE and is described by:[70]

$$I_R = I_0 \exp\left(\frac{\beta_{PFE} V^{1/2}}{kTd^{1/2}}\right) \quad (16)$$

Table 1. The electrical parameters of the SD and MIS devices. Some of the reported Φ_{BH} values of InP-based MIS/MOS type devices are given for comparison.

Parameters	SD	MIS	Reported Φ_{BH} (eV) from the literature
I-V method	0.57	0.64	**Present work**
Φ_{BH} (eV)			
'n'	1.31	1.27	0.62 eV for Au/Al_2O_3/n-InP diode,[12] 0.50 eV for Ag/TiO_2/n-InP diode,[13] 0.74 eV for Au/Cr_2O_3/p-Si MIS diode,[16] 0.69 eV for Au/ZrO_2/n-InP MIS diode,[23] 0.66 eV for Ag/SnO_2/n-InP diode,[25] 0.71 eV for Au/p-GO/n-InP/Au-Ge diode,[66] 0.71 eV for Au/rGO/n-InP/In diode,[69] and 0.47 eV for Pt/ZnO/InP diode[70]
Cheung's procedure dV/dlnI versus I	3.0	19.5	
R_S (kΩ)			
'n'	2.23	2.08	
H (I) versus I	0.53	0.61	
Φ_{BH} (eV)			
R_S (kΩ)	2.2	18.1	
Norde method	3.5	28.0	
R_S (kΩ)			
Φ_{BH} (eV)	0.56	0.64	
C-V method	0.61	0.81	
Built-in potential (V_{bi})			
Φ_{BH} (eV)	0.67	0.86	
Interface state density (N_{SS}) $eV^{-1}cm^{-2}$	7.66×10^{14} to 1.02×10^{13}	1.09×10^{13} to 2.96×10^{10}	

and for the SE

$$I_R = AA^* T^2 \, exp\left(-\frac{\Phi_S}{kT}\right) exp\left(\frac{\beta_{SE} V^{1/2}}{kTd^{1/2}}\right) \quad (17)$$

here d is the depletion width, β_{PFE} is the Poole-Frenkel and β_{SE} is the Schottky field lowering coefficients, respectively. The hypothetical values for β_{PFE} and β_{SE} are stated by:

$$2\beta_{SE} = \beta_{PFE} = \left(\frac{q^3}{\pi\varepsilon_0\varepsilon_r}\right)^{1/2} \quad (18)$$

The β_{PFE} is normally double the value of the β_{SE}. The plot of $\ln(I_R)$ versus $V_R^{1/2}$ for the SD and MIS is presented in Figure 8b. The hypothetical field-lowering coefficients (β_{PFE} and β_{SE}) for PFE and SE, along with the slope magnitudes experimentally determined for SD and MIS are presented in **Table 2**. Two different zones (area I: lower bias region and area II: higher bias region) are observed in Figure 8b for SD and MIS, suggesting two different RCMs under reverse bias regions. The slope values (Figure 8b) determined practically in area I are consistent with the hypothetical values of PFE for both SD and MIS, confirming that PFE is the dominant mechanism in this region. The PFE process may be attributed to large structural defects or trap states in the interface layer, which enhances the trapping-detrapping of charge carriers.[72] The slope values practically determined (Figure 8b) in area II are closer to the hypothetical SE values for both SD and MIS, revealing that SE governs the RCM in this region. In SE, RCM occurs through the contact interface rather than the bulk material.[73]

The analysis of the data on PFE and SE indicates that an additional mechanism for current conduction is likely exists. Therefore, we have applied the trap-assisted tunneling (TAT) mechanism. The *I–V* relationship for the TAT mechanism can be described as:[74]

$$I = B \exp\left[-\frac{8\pi\sqrt{2qm^*}(\Phi_t)^{3/2}}{3hE}\right] \quad (19)$$

where B is a constant, h is the plank constant, m* is the effective mass of electrons and its value is 0.078 m_0 for n-InP,[75] m_0 is the electron's rest mass of the electron. If Equation (19) is arranged, the following equation can be written as:

$$\ln(I) = -\frac{8\pi\sqrt{2qm^*}(\Phi_t)^{\frac{3}{2}}}{3hE} + \ln B \quad (20)$$

According to Equation (20), the plot of ln(I) versus 1/E is linear, with a negative slope. Figure 8c illustrates the ln(I) versus 1/E curves for SD and MIS at room temperature. In the high electric field range, the curves are linear, indicating negative slopes. This suggests that the dominant RCM for both SD and MIS is TAT. However, in the low electric field range, the curves become curved, indicating that TAT is not the dominant RCM in this region.

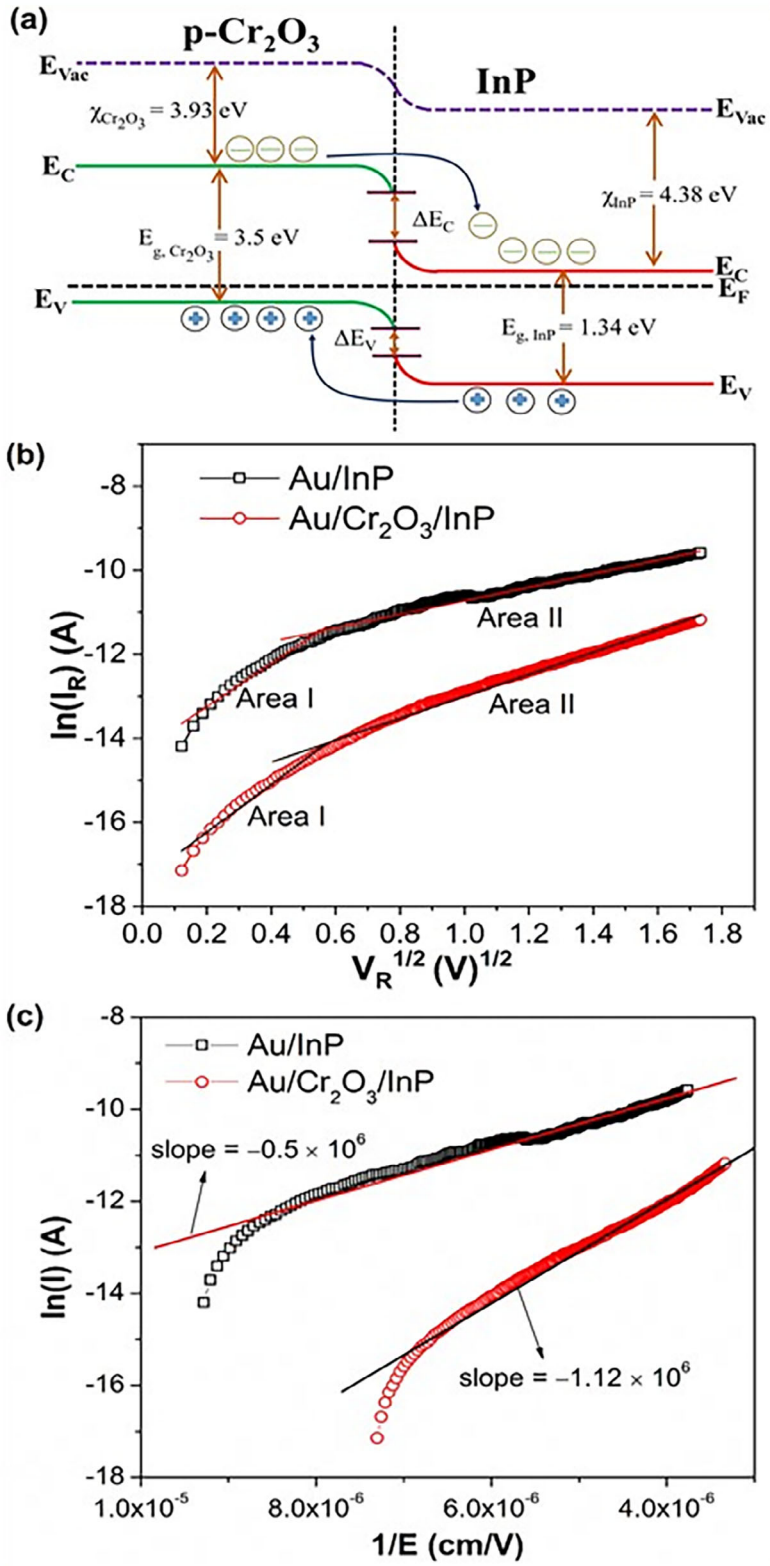

Figure 8. a) Schematic energy band diagram of the $Au/Cr_2O_3/InP$ interface. b) The $\ln(I_R)$ versus $V_R^{1/2}$ plot of the Au/InP SD and $Au/Cr_2O_3/InP$ MIS devices. c) Plot of reverse bias ln (I)- 1/E characteristics for the Au/InP SD and $Au/Cr_2O_3/InP$ MIS.

Table 2. Hypothetical and experimental slope values of β_{PFE} and β_{SE} field lowering coefficients of the SD and MIS devices.

Structures	Hypothetical values eV $m^{1/2}$ $V^{-1/2}$	Experimental values eV $m^{1/2}$ $V^{-1/2}$
Au/undoped-InP SD	$\beta_{PFE} = 2.24 \times 10^{-5}$	2.32×10^{-5} area I
	$\beta_{SE} = 1.12 \times 10^{-5}$	0.42×10^{-5} area II
Au/Cr_2O_3/undoped-InP MIS	$\beta_{PFE} = 2.19 \times 10^{-5}$	3.89×10^{-5} area I
	$\beta_{SE} = 1.09 \times 10^{-5}$	1.79×10^{-5} area II

3. Conclusions

Summarizing the results, we demonstrated significant enhancement in the electrical properties and performance of Au-Cr_2O_3-InP MIS devices, where the effect of the Cr_2O_3 interfacial layer is notable in electrical characteristics. Cr_2O_3 films were deposited on InP substrates using a simple, low-temperature, economically viable and chemical method. The surface morphology, structural and chemical bonding characterization made using AFM, FESEM, XRD, FTIR, and Raman spectroscopy revealed the high structural quality and phase pure formation of hexagonal Cr_2O_3. The optical measurements coupled with structural studies demonstrated that the Cr_2O_3 layer without impurities had a bandgap of ≈3.5 eV. To determine the effect of the Cr_2O_3 interfacial layer, the electrical characteristics of Au-InP devices with and without the Cr_2O_3 interfacial layer were evaluated using detailed *I–V* and C-V measurements. The results reveal a better qualifying property for MIS than for SD, where the remarkable effect of Cr_2O_3 is reflected in the leakage current, which is significantly lower in MIS compared to SD. It is evident that the addition of the Cr_2O_3 interlayer alters the potential barrier of the SD and increases the Φ_{BH}. The Φ_{BH} obtained from *I–V*(0.64 eV)/C-V (0.86 eV) for the MIS is greater than SD (0.57 eV (*I–V*)/0.67 eV (C-V)). Furthermore, the log (I) V plot also indicated the effect of Cr2O3 interlayer on Φ_{BH}. The results of Cheungs and Nordes' methodologies are comparable, suggesting that the outcomes are reliable and consistent. Since the N_{SS} for MIS is lower than SD, it is clear that the Cr_2O_3 interlayer contributes significantly to the reduction of N_{SS}. According to analyses, the Schottky emission controls the higher bias region in both SD and MIS, whereas the Poole-Frenkel emission regulates the reverse conduction mechanism in the lower bias region. The results of these studies demonstrated the versatile nature of the Cr_2O_3 layer for developing and creating electrical device technologies.

4. Experimental Section

Interlayer Deposition and Device Fabrication: The Au/undoped-InP Schottky diodes (SD) and Au/Cr_2O_3/InP metal/interface layer/ semiconductor (MIS) Schottky-type diodes were designed on an undoped-InP surface. The series of steps involved in the deposition and fabrication of devices are presented schematically in Figure S3 (Supporting Information). The scrubbing procedure for the undoped-InP surface was monitored as mentioned in the earlier work.[76] Furthermore, indium (In) with 50 nm thickness was thermally evaporated on the uneven InP surface as an ohmic contact and then exposed to annealing at 375 °C for 60 s using a rapid thermal annealing system in the N_2 environment. This ensures homogeneous and uniform In contact on the back of the InP substrate. Subsequently, the Cr_2O_3 solution (bought from Nano Shel with 99.99% purity and concentration: 5 mg ml^{-1} in water) was coated on the InP surface using the spin-coating technique (Model No: Laurell WS-650MZ-23NPP) (acceleration rate: 1200 rpm s^{-1} and spin rate: 4500 rpm, duration: 60 s). The deposition was repeated three times to obtain the required film thickness. Later, the spin-coated Cr_2O_3 films were dried in air on a hot plate at 250 ° C for 1 h. The thickness of the Cr_2O_3 film determined using a FESEM was ≈71 nm. Lastly, gold (Au) with a thickness of 30 nm was coated on top of Cr_2O_3 film as a Schottky diode. Au deposition was carried out at a base pressure of 2.1×10^{-5} mbar. Subsequently, the optical, structural and chemical characteristics of Cr_2O_3 were monitored by UV–vis, FTIR analysis, Raman spectroscopy, XRD, and XPS procedures.

Material Characterization—Atomic Force Microscopy (AFM) and Field Emission Scanning Electron Microscopy (FESEM) Measurements: The surface morphology and cross sectional properties of Cr_2O_3thin films deposited on InP substrates were examined using atomic force microscopy (AFM) and field emission scanning electron microscopy (FESEM). The measurements were conducted with an AFM (Nanosurf, Switzerland, Model: Nanosurf AFM) and a FESEM (Thermo Fisher, Model: FEI QUANTA 250 FEG, operated at 20 kV) to assess the surface roughness and thickness of the Cr_2O_3 thin film on the InP substrate.

Material Characterization—X-Ray Diffraction (XRD): Crystal structure and phase analysis of the spin-coated Cr_2O_3 films was performed using X-ray diffraction measurements. XRD measurements were made using Cu K_α radiation with $\lambda = 1.5418$ Å (Rigaku – Japan, Smart Lab). Measurements were made at room temperature, and the set scan rate was 0.02° per second.

Material Characterization—Fourier Transform Infrared Spectroscopy (FTIR): The structural quality and chemical bonding in Cr_2O_3 films was probed by FTIR measurements. Measurements were made in an FTIR spectrometer (IRAffinity-1S Fourier Transform Infrared Spectroscopy manufactured by Shimadzu in Kyoto, Japan).

Material Characterization—Raman Spectroscopy: The Cr_2O_3 thin film samples were also probed by Raman spectroscopic measurements to understand the chemical bonding. Measurements were made at room temperature using a Renishaw confocal Raman instrument using an excitation laser with a wavelength of 532 *nm*. The Raman spectra were recorded at four different locations on the sample for 50 s for three measurements summed and averaged for each measurement location.

Material Characterization—X-Ray Photoelectron Spectroscopy (XPS): Understanding the effects of interlayers and their surface chemistry is quite important. In the previous research,[77,78] it was made possible to understand the surface chemistry of a wide variety of oxide films with and without dopants by XPS characterization. Consequently, the spin-coated Cr_2O_3 films were analyzed using the previously established methods. For the sake of clarity and understanding, a brief description of the XPS measurements and analytical techniques was provided. XPS measurements were performed in an XPS chamber (Thermos Scientific Inc.). A monochromatic Al Kα X-ray source (1486.6 eV) was used. An electron emission angle of 54.7 ° was used with respect to the normal surface, while no sputtering of the surface was performed prior to the XPS measurements. All measurements were made at a base pressure of 1×10^{-9} Torr and the charge neutralizer were used. The survey and high-resolution (HR) scans were performed at pass energies of 160 and 40 eV, respectively. The high-resolution XPS spectra of the Cr, O, In, and P core levels were obtained and analyzed to understand the surface chemistry and electronic structure of the Cr_2O_3 films. Standard procedures[77–79] were employed to extract information on the chemical valence states of the respective elements. The relative sensitivity factors (RSF) for Cr 2p and O 1s core levels were used to determine the chemical composition, specifically to validate the O/Cr ration in the films deposited. Using the peak fits and RSF (Cr 2p: 10.6041 and O 1s: 2.93), the surface chemical composition of the films were determined while the binding energy of the core level peaks were analyzed to determine their chemical valence states.

Optical Characterization: Spectrophotometry measurements were made on Cr_2O_3 films using a spectrophotometer (JASCO FLH-740UV-Vis-NIR). For spectroscopic investigation of transparent Cr_2O_3, monochromatic light ranging from near-infrared to deep UV was utilized to measure transmittance. The baseline measurement was first established by

measuring the transmitted intensity on a bare substrate. The transmittance of the film was then given by normalizing the measured transmitted light intensity to that of the baseline measurement. Spectrophotometry measurements were made in the wavelength range of 300–1000 nm, which was more than sufficient to analyze and determine the bandgap of Cr_2O_3 films.

Device Characterization: Finally, after thoroughly understanding the structure, chemical bonding, surface chemistry, and optical properties of Cr_2O_3 films, the electrical properties of Au/InP SD and Au/Cr_2O_3/InP MIS devices were evaluated. The effect of the Cr_2O_3 interlayer on electrical properties and performance was studied using current–voltage (*I–V*) and capacitance-voltage characteristics. *I–V* measurements were made using an Agilent 4156C Semiconductor Parameter Analyzer, while C-V measurements were made using HP 4248 LCR meter. The C-V measurements were made at a constant frequency of 1 MHz. All measurements were made at room temperature.

Supporting Information

Supporting Information is available from the Wiley Online Library or from the author.

Acknowledgements

The authors of The University of Texas at El Paso acknowledge, with pleasure, support from the National Science Foundation (NSF) with NSF-PREM grant #DMR-1827745.

Conflict of Interest

The authors declare no conflict of interest.

Data Availability Statement

The data that support the findings of this study are available from the corresponding author upon reasonable request.

Keywords

charge transport process, Cr_2O_3, electrical properties, InP, interfaces, structure

Received: January 19, 2025
Revised: March 28, 2025
Published online: May 1, 2025

[1] J. Wang, Q. Yao, C.-W. Huang, X. Zou, L. Liao, S. Chen, Z. Fan, K. Zhang, W. Wu, X. Xiao, C. Jiang, W. Wei, *Adv. Mater.* **2016**, *28*, 8302.
[2] H. Schlicke, R. Maletz, C. Dornack, A. Fery, *Small* **2024**, *20*, 2403502.
[3] C. Xie, F. Yan, *Small* **2017**, *13*, 1701822.
[4] F. E. Cimilli Çatır, *Semicond. Sci. Technol.* **2020**, *35*, 035023.
[5] D. S. Schulman, A. J. Arnold, S. Das, *Chem. Soc. Rev.* **2018**, *47*, 3037.
[6] R. Agarwal, *Small* **2008**, *4*, 1872.
[7] J. Chen, J. Lv, Q. Wang, *Thin Solid Films* **2016**, *616*, 145.
[8] M. Smit, K. Williams, J. van der Tol, *APL Photonics* **2019**, *4*, 050901.
[9] G. Almeida, R. F. Ubbink, M. Stam, I. du Fossé, A. J. Houtepen, *Nat. Rev. Mater.* **2023**, *8*, 742.
[10] W. Zhang, S. Ding, W. Zhuang, D. Wu, P. Liu, X. Qu, H. Liu, H. Yang, Z. Wu, K. Wang, X. W. Sun, *Adv. Funct. Mater.* **2020**, *30*, 2005303.
[11] P. Liu, Y. Lou, S. Ding, W. Zhang, Z. Wu, H. Yang, B. Xu, K. Wang, X. W. Sun, *Adv. Funct. Mater.* **2021**, *31*, 2008453.
[12] H. Kim, D. H. Kim, S. Ryu, B. J. Choi, *Vacuum* **2017**, *144*, 256.
[13] H. Kim, D. H. Kim, B. J. Choi, *AIP Adv.* **2018**, *8*, 025211.
[14] A. Gutierrez-Aitken, in *Compr. Semicond. Sci. Technol.*, New Jersy **2011**, *5*, 114.
[15] D. Korucu, S. Duman, *Thin Solid Films* **2013**, *531*, 436.
[16] N. A. Al-Ahmadi, *Mater. Res. Express* **2020**, *7*, 032001.
[17] L. J. Brillson, C. F. Brucker, A. D. Katnani, N. G. Stoffel, R. Daniels, G. Margaritondo, *J. Vac. Sci. Technol.* **1982**, *21*, 564.
[18] A. K. Bilgili, R. Cagatay, M. K. Ozturk, M. Ozer, *Silicon* **2022**, *14*, 3013.
[19] I. A. Digdaya, G. W. P. Adhyaksa, B. J. Trzes´niewski, E. C. Garnett, W. A. Smith, *Nat. Commn.* **2017**, *8*, 15968.
[20] I. Y. Erdogan, O. Gullu, *Appl. Surf. Sci.* **2010**, *256*, 4185.
[21] Y. S. Ocak, A. A. Issa, M. F. Genisel, A. Tombak, T. Kilicoglu, *J. Phys. Conf. Ser.* **2016**, *707*, 012026.
[22] O. Gullu, A. Tataroglu, *Phys. Scr.* **2023**, *98*, 015837.
[23] N. Balaram, M. Siva Pratap Reddy, V. Rajagopal Reddy, C. Park, *Thin Solid Films* **2016**, *619*, 231.
[24] N. Balaram, V. Rajagopal Reddy, P. R. Sekhar Reddy, V. Janardhanam, C. J. Choi, *Vacuum* **2018**, *152*, 15.
[25] M. A. Salari, M. Odabas, B. Guzeldir, M. Saglam, *Int. J. Sci. Eng. Res.* **2019**, *10*, 52.
[26] A. K. Bilgili, *Braz. J. Phys.* **2023**, *53*, 22.
[27] S. Mahato, J. Puigdollers, *Phys. B: Phys. Condens. Matter* **2018**, *530*, 327.
[28] S. Mahato, D. Biswas, L. G. Gerling, C. Voz, J. Pulgdollers, *AIP Adv.* **2017**, *7*, 085313.
[29] S. Ashajyothi, V. Rajagopal Reddy, C. J. Choi, *J. Mater. Sci.: Mater. Electron.* **2023**, *34*, 1482.
[30] D. Das, F. Sanchez, D. J. Barton, S. Tan, V. Shutthanandan, A. Devaraj, C. V. Ramana, *Adv. Mater. Technol.* **2023**, *8*, 2300014.
[31] K. J. Saji, K. Tian, M. Snure, A. Tiwari, *Adv. Electron. Mater.* **2016**, *2*, 1500453.
[32] K. Zhou, G. Shang, H. H. Hsu, S.-T. Han, V. A. L. Roy, Y. Zhou, *Adv. Mater.* **2023**, *35*, 2207774.
[33] S. Dabaghmanesh, R. Saniz, E. Neyts, B. Partoens, *RSC Adv.* **2017**, *7*, 4453.
[34] S. Mann, B. Prakash, *Wear* **2000**, *240*, 223.
[35] A. Cellard, V. Garnier, G. Fantozzi, G. Baret, P. Fort, *Ceram. Inter.* **2009**, *35*, 913.
[36] I. Veremchuk, M. O. Liedke, P. Makushko, T. Kosub, N. Hedrich, O. V. Pylypovskyi, F. Ganss, M. Butterling, R. Hubner, E. Hirschmann, A. G. Attallah, A. Wagner, K. Wagner, B. Shields, P. Maletinsky, J. Fassbender, D. Makarovet, *Small* **2022**, *18*, 2201228.
[37] P. Rickhaus, O. V. Pylypovskyi, G. Seniutinas, V. Borras, P. Lehmann, K. Wagner, L. Zaper, P. J. Prusik, P. Makushko, I. Veremchuck, T. Kosub, R. Hubner, D. D. Sheka, P. Maletinsky, D. Makarov, *Nano Lett.* **2024**, *24*, 13172.
[38] P. Makushko, T. Kosub, O. V. Pylypovskyi, N. Hedrich, J. L. A. Pashkin, S. Avdoshenko, R. Hubner, F. Ganss, D. Wolf, A. Lubk, M. O. Liedke, M. Butterling, A. Wagner, K. Wagner, B. J. Shields, P. Lehmann, I. Ceremchuk, J. Fassbender, P. Maletinsky, D. Makarov, *Nat. Commun.* **2022**, *13*, 6745.
[39] Y.-H. Qiu, X.-S. Qiu, C. W. Huang, *ACS Appl. Electron. Mater.* **2024**, *6*, 7003.
[40] A. Joseph, J. Sunny, T. Thomas, M. R. Anantharaman, *ChemistrySelect* **2022**, *7*, 202203049.
[41] G. Zhao, T. Wen, J. Zhang, J. Li, H. Dong, X. Wang, Y. Guo, W. Hu, *J. Mater. Chem. A* **2014**, *2*, 944.
[42] S. Choi, M. Bonyani, G. Sun, J. K. Lee, S. K. Hyun, C. Lee, *Appl. Surf. Sci.* **2018**, *432*, 241.
[43] M. M. Abdullah, F. M. Rajab, S. M. Al-Abbas, *AIP Adv.* **2014**, *4*, 027121.
[44] H. Ma, Y. Xu, Z. Rong, X. Cheung, S. Gao, X. Zhang, H. Zhao, L. Huo, *Sens. Actuators B: Chem.* **2012**, *174*, 325.

[45] I. R. Grant, *III–V Compound Semiconductors: Growth. Encyclopedia of Materials: Science and Technology*, Elsevier, Amsterdam **2001**, p. 1441.
[46] S. Ponmudi, R. Sivakumar, C. Sanjeeviraja, C. Gopalakrishnan, T. Okamoto, *J. Mater. Sci.: Mater. Electron.* **2020**, *31*, 10123.
[47] V. Janardhanam, A. Ashok Kumar, M. Bhaskar Reddy, V. Rajagopal Reddy, P. Narasimha Reddy, A. K. Balamurugan, A. K. Tyagi, *Phys. Status. Solidi. A* **2009**, *11*, 2658.
[48] C. V. Ramana, O. M. Hussain, R. Pinto, C. M. Julien, *Appl. Surf, Sci.* **2003**, *207*, 135.
[49] L. N. Ambadi, A. Navid, V. Shutthanandan, C. V. Ramana, *Adv. Funct. Mater.* **2024**, *34*, 2316379.
[50] C. V. Ramana, A. Ait-Salah, S. Utsunomiya, F. Gendron, C. M. Julien, *Chem. Mater.* **2007**, *55*, 5754.
[51] P. Bhardwaj, J. Singh, R. Kumar, R. Kumar, V. Verma, *Solid State Sci.* **2021**, *115*, 106581.
[52] J. Mougin, T. Le Bihan, G. Lucazeau, *J. Phys. Chem. Solid* **2001**, *62*, 553.
[53] S. Khamlich, E. Manikandan, B. Ngom, J. Sithole, O. Nemraoui, I. Zorkani, R. McCrindle, N. Cingo, M. Maaza, *J. Phys. Chem. Solids* **2011**, *72*, 714.
[54] Z. Cao, C. Zuo, *RSC Adv.* **2017**, *7*, 40243.
[55] M. Guo, Q. Liu, P. Zhao, J. Han, X. Li, Y. Ha, Z. Fu, C. Song, N. Ji, C. Liu, D. Ma, Z. Li, *Chem. Eng. J.* **2019**, *361*, 830.
[56] A. Bumajdad, S. Al-Ghareeb, M. Madkour, F. A. Sagheer, *Sci. Rep.* **2017**, *7*, 14788.
[57] L. Yang, T. Wang, Y. Zou, H. L. Lu, *Nanoscale Res. Lett.* **2017**, *12*, 339.
[58] J. Tacu, *Mater. Res. Bull.* **1968**, *3*, 37.
[59] M. Tabbal, S. Kahwaji, T. C. Christidis, B. Nsouli, K. Zahraman, *Thin Solid Films* **2006**, *515*, 1976.
[60] M. S. Mehr, L. Aarik, T. Jogiaas, A. Tarre, A. Kasikov, K. Roosalu, H. Mandar, *J. Alloys Compd.* **2023**, *968*, 172041.
[61] V. R. Reddy, C. J. Choi, *J. Alloys Compd.* **2020**, *823*, 153775.
[62] E. H. Rhoderick, R. H. Williams, *Metal-Semiconductor Contacts*, 2nd ed., Clarendon Press, Oxford **1988**.
[63] R. T. Tung, *Phys. Rev. B* **1992**, *45*, 13509.
[64] S. K. Cheung, N. W. Cheung, *Appl. Phys. Lett.* **1986**, *49*, 85.
[65] H. Norde, *J. Appl. Phys.* **1979**, *50*, 5052.
[66] H. C. Card, E. H. Rhoderick, *J. Phys. D: Appl. Phys.* **1971**, *4*, 1589.
[67] S. M. Sze, *Physics of Semiconductor Devices*, Wiley, New York **1981**.
[68] A. Baltakesmez, *Vacuum* **2019**, *168*, 108825.
[69] F. Catir, *J. Mater. Sci.: Mater. Electron.* **2020**, *32*, 611.
[70] H. Kim, M. J. Jung, B. J. Choi, *J. Mater. Sci. Mater. Electron.* **2021**, *32*, 22792.
[71] J. M. Grady, S. Yamashita, S. Kano, H. Yang, H. Abe, *Radiat. Phys. Chem.* **2021**, *180*, 109240.
[72] J. G. Simmons, *Phys. Rev.* **1967**, *155*, 657.
[73] A. C. Varghese, C. S. Menon, *Eur. Phys. J. B* **2005**, *47*, 485.
[74] C. S. Guclu, A. F. Ozdemir, D. A. Aldemir, S. Altindal, *J. Mater. Sci. Mater. Electron.* **2021**, *32*, 5624.
[75] C. W. Wilmsen, *Physics and Chemistry of III-V Compound Semiconductor Interfaces*, Plenum Press, New York and London **1985**.
[76] V. Rajagopal Reddy, A. Usha Rani, S. Ashajyothi, D. Surya Reddy, A. Ashok Kumar, *J. Mol. Struct.* **2023**, *1294*, 136490.
[77] C. V. Ramana, D. Das, G. Gutierrez, F. S. Manciu, V. Shutthanandan, *J. Mater. Sci.* **2022**, *57*, 11170.
[78] C. V. Ramana, M. Bandi, A. N. Nair, F. S. Manciu, S. Sreenivasan, V. Shutthanandan, *ACS Appl. Energy Mater.* **2021**, *4*, 1313.
[79] V. V. Atuchin, A. V. Kalinkin, V. A. Kochubey, V. N. Kruchinin, R. S. Vemuri, C. V. Ramana, *J. Vac. Sci. Technol. A* **2011**, *29*, 021004.